

# Thermal modelling of the Larderello geothermal field (Tuscany, Italy)

Bruno Della Vedova · Claudio Vecellio ·  
Stefano Bellani · Umberta Tinivella

Received: 27 February 2007 / Accepted: 6 September 2007  
© Springer-Verlag 2007

**Abstract** We present a 3-D thermal model of the Larderello geothermal field (Tuscany) to evaluate (1) the extent and contribution of the heat transfer mechanisms (conduction vs. convection) at the intermediate-upper crust levels, (2) the variability of the heat and mass fluxes entering from below and (3) the crucial role of the formation permeability. The model, composed by three main layers, considers the upper 10 km of the crust to better constrain the simulations with experimental data from borehole, fluid inclusion studies and hypocentral distributions. Several sets of simulations were carried out with different bottom boundary temperatures and different formation permeabilities for the two deeper layers. The results indicate that the present temperature ( $T$ ) and pressure distributions in the Larderello field require deep reservoir rocks with higher permeability than the overlying capping units and underlying intermediate crust. Permeability values of 1 mDarcy for the reservoir rocks are enough to allow fluid convection, if the temperature at 10 km depth is as high as  $500 \pm 50^\circ\text{C}$ . The presence of localized zones with formation permeability 50–100 times higher than the surrounding rocks strongly favours the migration of overpressurized fluids, which episodically break through the

overburden, feeding the presently exploited geothermal fields.

**Keywords** Larderello geothermal field · Convective heat transfer · Fluid over-pressure · K-horizon · 3-D thermal modelling

## Introduction

The lithospheric extension and the upper mantle doming of the Tuscan-Tyrrhenian domain are among the most remarkable and active tectonic processes within the entire Alpine-Mediterranean deformation area. They have been active since Miocene times (Carmignani et al. 1994; Brunet et al. 2000) and are likely sustained by mass and heat fluxes from the upper mantle, as suggested by the intense tectonic and volcanic activity, associated to extremely high and variable surface heat flux anomalies (Della Vedova et al. 2001). All these processes document a predominant heat transfer mechanism by vertical mass flow, which accumulates large amount of geothermal resources at accessible depths in the upper crust.

Despite intensive exploration and exploitation drilling programs, carried out in Tuscany, the nature, physical properties and heat transfer mechanisms of the intermediate and lower crust and of the upper mantle are still debated. The reconstruction of the temperature distribution with depth ( $T$ - $z$ ) in this area is crucial for the understanding of the nature and physical properties of the lithospheric units, as well as for the comprehension of the rheology and future evolution of the extended areas.

To understand the crustal structures and their relationship in the geothermal fields of Southern Tuscany, three seismic lines (CROP 18A, 18B, and CROP 03, Fig. 1) were

---

B. Della Vedova (✉) · C. Vecellio  
Dipartimento di Ingegneria Civile e Ambientale,  
Università di Trieste, Via Valerio 10, 34127 Trieste, Italy  
e-mail: dellavedova@units.it

S. Bellani  
Istituto di Geoscienze e Georisorse, CNR,  
Via Moruzzi 1, 56124 Pisa, Italy

U. Tinivella  
Istituto Nazionale di Oceanografia e Geofisica Sperimentale,  
OGS, Borgo Grotta Gigante 42/C, 34010 Sgonico (Trieste), Italy

acquired on land in the frame of the CROsta Profonda (CROP) project (Scrocca et al. 2003). Along with wide-angle reflection and refraction deep seismic soundings (DSS data; Giese et al. 1981), the CROP seismic lines give information about the crustal structure of the geothermal province. These seismic reflection profiles cross specifically the Larderello and Monte Amiata geothermal fields. They have been recently reprocessed in order to better characterize the crustal and upper mantle structures of the Tuscan geothermal area. The results (Accaino et al. 2005, 2006; Tinivella et al. 2005) show a remarkable definition of the geometry of the “K-horizon” (the main marker of this region as defined by Batini et al. 1978), a second deeper and more continuous similar horizon (here after called  $K_2$  horizon), sub-vertical mantle intrusions, strong reflectors in the lower crust and a discontinuous crust/mantle transition characterized by strong anisotropy in the seismic velocity (10–20%; Accaino et al. 2006). Accurate analyses of the seismic attributes suggest the presence of over-pressurized fluids below the K-horizon, down to about 10 km (Accaino et al. 2005). Fluid inclusion studies on rock samples coming from the Larderello geothermal field (Dini et al. 2005) allowed to discriminate the nature and thermodynamic characteristics of early fluid inclusions, as distinct from the late inclusions.

In this paper, we use the available geophysical data to constrain a set of preliminary convective thermal models, to be compared with the experimental borehole data and with the estimates of temperature ( $T$ ) and fluid pressures from fluid inclusions and deep seismic data. The main objectives were to evaluate (1) the heat transfer mechanisms at the intermediate-upper crust levels, (2) the variability of the heat and mass fluxes entering from below and (3) the crucial role of the formation permeability.

The thermal convection in porous/fractured media, including the temperature and pressure effects on

thermodynamic and transport properties, was specifically discussed by Straus and Schubert (1977).

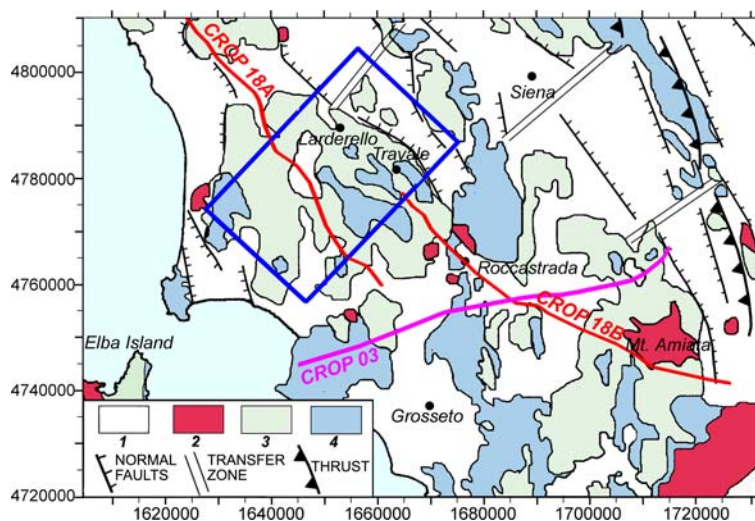
## Regional geologic setting

The Tuscan geothermal area is located in the inner side of the Northern Apennines (Fig. 1), where post-collisional extensional tectonics has been active since the Early Middle Miocene (Carmignani et al. 1994; Brunet et al. 2000), accompanied by a widespread Late Miocene-Quaternary magmatism (Serri et al. 1993) showing a progressive migration of the younger magmatic events in the E-ESE direction. The regional extension affecting the entire Western Mediterranean since Early–Middle Miocene, including the inner Northern Apennines (i.e., southern Tuscany), was coeval with the compression developing at the outer Apennines front, on the Adriatic side. The lithospheric extension was accompanied by mantle softening, crustal underplating and dike intrusion into the thinned continental crust.

The geologic and tectonic setting of southern Tuscany has been studied by several authors, including Decandia et al. (1998), Liotta et al. (1998), Brogi et al. (2003, 2005), and references therein.

The Larderello geothermal field in southern Tuscany produces superheated steam and fluids with a clear upper mantle isotopic signature (Magro et al. 2003); it is generally considered as a single, large hydrothermal system recharged by meteoric waters and heated from deep magmatic sources intruded into the thinned continental crust (Baldi et al. 1993). Although extrusive rocks are not outcropping in the Larderello area, felsic dikes and granitic bodies, encountered in boreholes at different depths, clearly indicate that magmas derive from mixing of mantle and crustal sources (Serri et al. 1993).

**Fig. 1** Simplified geological map of the Tuscan geothermal area (modified after Carmignani et al. 2004; Decandia et al. 1998). (1) Neoauctonous sediments (Lower Miocene-Pliocene); (2) Igneous rocks (Pliocene-Quaternary); (3) Alloctonous flysch *facies* units (Cretaceous-Eocene); (4) Potential reservoir formations (Tuscan Nappe, Tectonic Slices, Metamorphic Units; Precambrian–Late Triassic). Location of the main tectonic features are shown. CROP profiles and the position of the 3-D numerical model are indicated



From late Miocene to late Pliocene, N–S to NW–SE trending normal faults were active in southern Tuscany, bordering several extensional basins (Pascucci et al. 1999) in a non-rotational setting (Mattei et al. 1996). The continuity of adjacent basins throughout southern Tuscany is interrupted by NE–SW strike-slip faults (Fig. 1). The Larderello field is characterised by normal faults with Apenninic direction (NW-trending, NE-dipping). Their geometry down to depths of 4/5 km is constrained by field, borehole, and seismic reflection data (Liotta and Ranalli 1999). Normal faulting within the Apennines and its per-Thyrrhenian foundered thrust belt leads to increasing vertical permeability, connectivity and fluid mixing in progressively larger and interconnected sectors of the stretched crust (Ghisetti and Vezzani 2002).

Seismic surveys detected a regional high-amplitude discontinuous reflector with local “bright spot” features (“K-horizon”), which marks the top of the reflective crust (Brogi et al. 2003 and references therein). It is largely accepted that the reflectivity of this horizon is related to fluids entrapped in fractured levels. The negative gravity anomaly in the area (Nicolich and Marson 1994) also accounts for the presence of over-pressurized fluids (Accaino et al. 2005), which induces a density decrease in the country rocks.

The K-horizon tops at about 3 km depth in correspondence of the Larderello and Mt. Amiata geothermal fields, deepening towards the peripheral areas. Accaino et al. (2005) and Tinivella et al. (2005) recognized a second highly reflective and more continuous horizon, beneath the K-horizon, named “K<sub>2</sub>”, that might hence be considered as

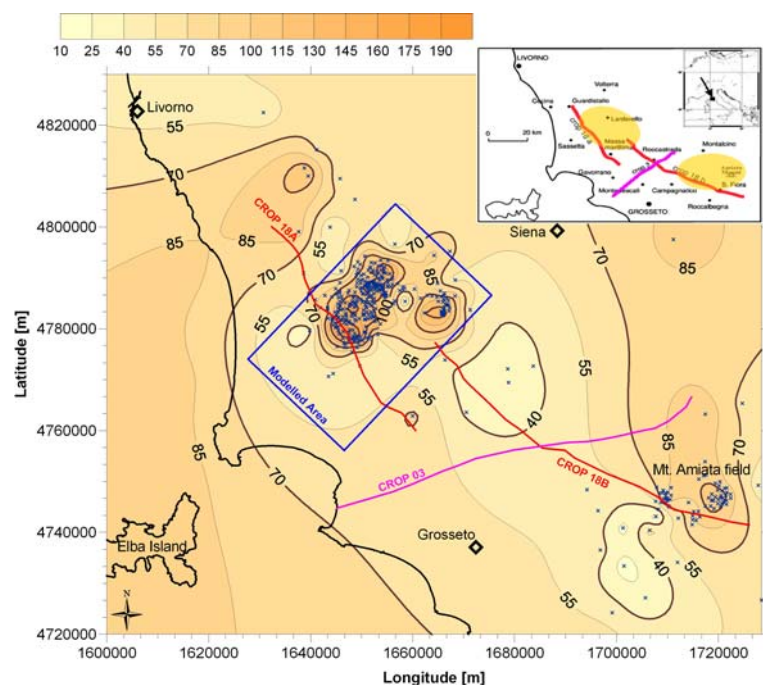
a regional sub-horizontal surface (at a depth of 8–9 km) likely more isothermal than the above K-horizon and already within the ductile zone ( $T$  in excess of 450°C).

## Geophysical data and crustal structures

The crustal structure of the Tuscan area is defined on the basis of the Deep Seismic Sounding (DSS) data (Giese et al. 1981; Nicolich 1989), body (Piomallo and Morelli 1998; Spakman 1990) and surface wave velocity tomography (Panza et al. 2003). DSS data define the top of the lower crust, at a depth from 12 to 16 km, on the basis of its  $V_p$  velocity of 6.8–7.3 km s<sup>-1</sup>. The crust-mantle boundary, imaged at 22–25 km depth (Locardi and Nicolich 2005; Nicolich 1989) is laminated and characterized by an anomalously low upper mantle velocity of 7.5–7.8 km s<sup>-1</sup>, likely corresponding to the culmination of the soft mantle upwelling beneath the geothermal province. The surface expression of this deeply rooted thermal process affects the whole Tuscan area (Della Vedova et al. 1991, 2001) and suggests a predominant heat transfer mechanism by upward mass flow, as shown in the thermal gradient map of Fig. 2.

Bouguer gravity anomalies, when computed with a reduction density of 2,670 kg m<sup>-3</sup>, evidence an excess of mass in the lower crust of the geothermal province, which is isostatically under-compensated (Velicogna et al. 1996; Marson et al. 1998). In addition, the Geoid elevation shows a steep gradient moving from western Tuscany towards Umbria-Marche regions (Barzaghi et al. 2002), confirming a strong lateral change in mass distribution at the depth of

**Fig. 2** Simplified map of the vertical geothermal gradient in the Tuscan area (mK m<sup>-1</sup>). Location of CROP profiles and geothermal wells (*crosses*) is shown. The *box* indicates the extension of the 3-D numerical model. Location of the Larderello and Monte Amiata fields is shown in the *inset* map



the crust-mantle boundary. On the other hand, when the Bouguer anomaly (Fig. 3) is computed with a reduction density of  $2,400 \text{ kg m}^{-3}$ , it shows a clear *deficit* of mass in the upper crust (Nicolich and Marson 1994; Baldi et al. 1995; Tinivella et al. 2005).

The emplacement of plutons (Acocella and Rossetti 2002), requires roof uplift of the crustal units to accommodate the ascent of granitic magmas; indeed, the Pliocene deposits of the Tuscan geothermal district experienced more than 600 m of regional uplift (Marinelli et al. 1993).

The seismic results of the CROP 18A transect (Fig. 4) through the Larderello field (Accaino et al. 2005) significantly improved the knowledge on the stretched continental crust underlying the Tuscan area. It is characterized by: a complex and structured upper part, an intermediate less (or poorly) reflective crust and a highly reflective mid-lower crust, often bottomed by a laminated crust-mantle boundary at 22–24 km depth. The K-horizon reaches minimum depths of about 3–6 km in the geothermal areas, whereas it deepens to greater depths moving outwards. The character of the high-amplitude reflectors within the middle and lower crust ( $K_2$  horizon and others deeper) is sometimes stronger than the signature of the well-known shallower K-horizon. The amplitude of these deep reflectors drops off in the proximity of the Larderello and Monte Amiata geothermal fields, where, instead, the K-horizon above is well imaged. Non-conventional analysis (such as AVO; Accaino et al. 2005) on the seismic data suggests that the upper remarkable K-horizon beneath the Larderello and Monte Amiata geothermal fields can be

associated with fluid over-pressure conditions. The  $K_2$  horizon, instead, is a deeper and a more regional reflecting interval, compatible with a lithologic change. However, the shape and depth of this structure, as well as the associated micro-earthquakes hypocenters down to 8 km depth (Vannorio et al. 2004), suggest that the  $K_2$  horizon might be a reasonable image of the brittle-ductile transition.

The reflectivity associated with lithologic changes beneath  $K_2$  can be explained by the presence of mantle intrusions into the extended deep continental crust. The intrusion of mantle-derived magmas has been studied in depth in the Ivrea-Verbano zone by Sinigoi et al. (2003). The heat input at the base of the crust induces crustal erosion and underplating which triggers partial melting of lower crust granulite *facies*. The upward migration of melts increases the density of the depleted restitic rocks, which could provide a laminated seismic image, because of repeated episodes of dikes/sills intrusion. A sharp distinction between denser materials and lighter melts/rocks explains the presence of alternating impedance and observed reflectivity.

The rising of the partial melting front from the lower crust affects the overlying crustal rocks (anatexis), with production of granitic melts quickly migrating to higher crustal levels. Fluid over-pressure occurs in reservoir rocks when capped by impermeable layers; the strong reflective K-horizon marks the transition between the deep reservoir and the cap rocks.

Possible diffused intrusions, likely distributed laterally (sills) and at depth, are likely present below the

**Fig. 3** Bouguer gravity anomalies (in mGal) of the Tuscan geothermal area (modified after Baldi et al. 1995). Location of CROP profiles and 3-D numerical model is shown

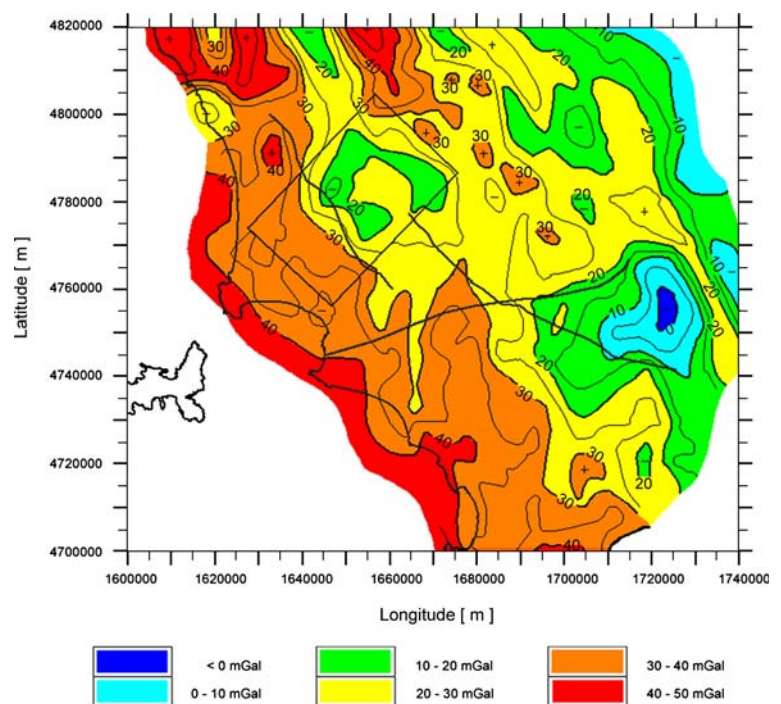
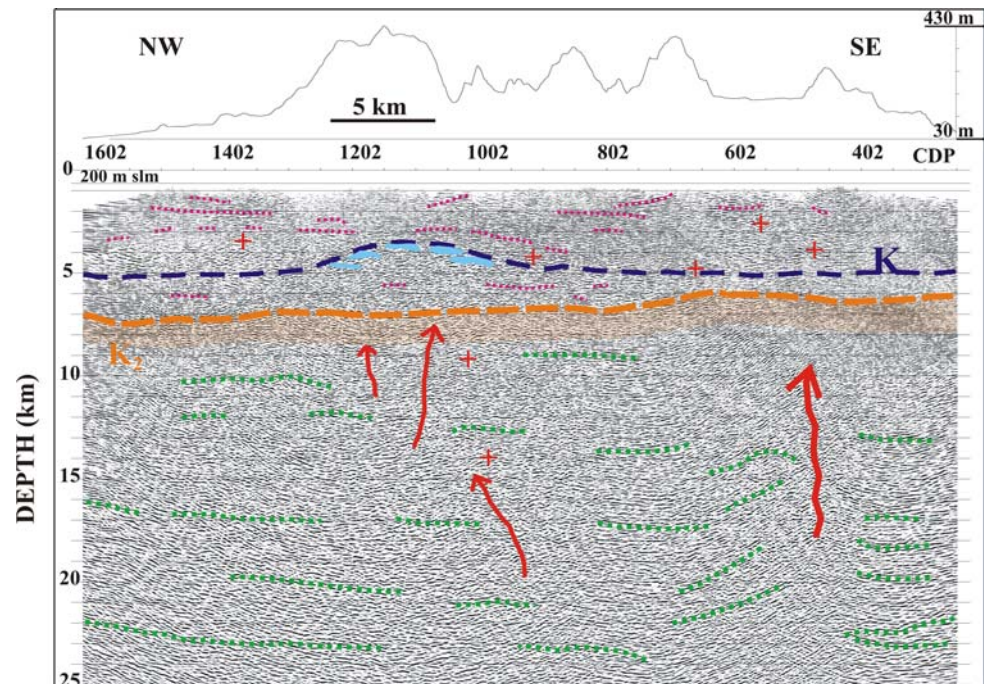


**Fig. 4** Interpreted post-stack depth migrated CROP 18A across the Larderello field, showing K horizons, evidence of fluid traps (*blue spots*), vertical conduits (*arrows*), magmatic intrusions (*crosses*) and deep reflections (*dotted lines*). Modified after Accaino et al. (2005, 2006)



culmination of the K-horizon in correspondence of the Larderello field and also at the SE end of line 18-A (Fig. 4). The seismic analysis (Accaino et al. 2006) of the CROP 03 line, though external to the studied area (Fig. 1), confirmed that the lithosphere of the Tuscan geothermal province is affected by significant velocity and density changes, with geothermal fluids rising from great depths. From the theoretical modelling, the porosity in the overpressurized zones seems to have a value of the order of 5%, with a consequent decrease in density, which could partly explain the observed negative Bouguer anomalies (Nicolich and Marson 1994).

#### Thermal state of the area and isotopic constraints on the deep fluids

The lithospheric extension of the Tuscan region is clearly associated to intense heat flow anomalies, as imaged by surface heat flux measurements (Bellani et al. 2004), suggesting a predominant heat transfer mechanism by vertical mass flow. Groundwater flow and geothermal fluid circulation in the shallow levels of the crust are here important in generating very intense and laterally variable local heat flux anomalies (with values up to  $1 \text{ W m}^{-2}$ ). This high frequency component is superimposed on the regionally high background heat flux ( $150\text{--}200 \text{ mW m}^{-2}$ ) of the Tuscany-Latium area (Mongelli et al. 1989; Bellani and Della Vedova 2004), which reflects the transient effects of the recent lithospheric extension and associated intrusion of mantle derived magmas and fluids into the crust.

Temperature distribution in the Larderello area is well known down to depths of 4–4.5 km, thanks to the extensive drilling for geothermal exploration and exploitation. The thermal field shows a pronounced heterogeneity, with strong lateral  $T$  changes; at about 5 km depth we observe up to  $200^\circ\text{C}$   $T$  difference, over lateral distances of a few tens of km (Della Vedova et al. 2001; Bellani et al. 2004). This means that the whole area is still far from steady state conditions, though the geothermal activity dates back to at least 3.8 Ma (Gianelli and Laurenzi 2001). The progressive migration of the magmatic activity to the NE and the present geothermal activity of the Tuscan district likely require episodic input events of mass and energy, through the extensional brittle structures.

Two geothermal reservoir systems are industrially exploited in the Larderello field:

- the shallow reservoir system (at about 700–1,000 m depth), located in cataclastic rocks (evaporites) at the base of the sedimentary cover,
- the deep reservoir system, located in the fractured metamorphic basement (schists, phyllites, micaschists and gneisses) at depths ranging between 2,000 and 4,500 m.

The geothermal steam from permeable horizons within the metamorphic basement is characterised by temperatures well above  $300^\circ\text{C}$  and up to more than  $400^\circ\text{C}$  (Barelli et al. 2000).

Larderello is the preferential escape area in Tuscany for mantle-derived fluids, as indicated by the good agreement among relative maxima of He isotopic ratio  $R/R_a$ , where  $R_a$

represents its typical air value, positive heat flow anomalies and relative minima of the Bouguer gravity map (Magro et al. 2003).

The existence of relatively high  $R/R_a$  values in the Tuscan magmatic province is therefore, consistent with heat input at the base of the crust, anatexis of the overlying crustal rocks, production of granitic melts and their migration/intrusion into higher crustal levels.

At the brittle-ductile transition, the formation permeability decreases sharply (Bailey 1990; Fournier 1991), creating an impervious boundary (Kennedy and Van Soest 2006; Kennedy et al. 1997).  $^3\text{He}$  enriched fluids rising through vertical conduits homogenize with crustal derived fluids, enriched in radiogenic  $^4\text{He}$ , fill the permeable formations and spread horizontally, as a function of lateral permeability. The coexisting presence at the surface of both thermal and  $^3\text{He}$  positive anomalies, indicates that both energy and mass fluxes traverse the crust and issue at surface, producing in Larderello the strongest “mantle signature” (up to  $R/R_a$  values of 3, as compared to average crustal values around 0.02) among the volcanic areas of central Italy. The deep extensional structures (Acocella and Rossetti 2002; Vanorio et al. 2004; Accaino et al. 2005) beneath southern Tuscany are supposed to connect hydraulically the upper mantle with the intermediate/upper crust (Brogi et al. 2003; Bellani et al. 2005).

### Thermal and fluid dynamic modelling

On the basis of the CROP seismic data, integrated with existing geological and geophysical results, we set up a simplified 3-D thermal model to qualitatively evaluate the extent and relative importance of the main heat transfer mechanisms (conduction vs. convection), their space and time variability and the crucial role of the formation permeability ( $k$ ) at the intermediate-upper crustal levels. The simulated  $T$ - $z$  distribution could then be compared with the

experimental borehole data and with the estimates of  $T$  and fluid pressures from fluid inclusions and deep seismic data.

The model domain includes the whole Larderello geothermal field, extending over an area of  $42 \times 26$  km (see Fig. 1) and with a vertical thickness of 10 km, in order to include both K horizons. It is oriented according to the regional tectonic setting, with its short side along strike with the Apenninic orientation. It is composed by three main layers: the top layer represents heterogeneous rocks and terrains (mainly sedimentary rocks) above the upper K-horizon, the second layer represents the geological formations (intrusive and metamorphic rocks) in between the two K horizons (locally interested by over-pressurized fluids) and the third layer represents the crystalline basement between  $K_2$  and the model bottom. We deliberately chose to limit the total depth of the model to 10 km (about twice as much the maximum depth reached by boreholes in the Tuscan geothermal area), in order to control and validate the SHEMAT (see Appendix 1) numerical results with the geological and geophysical observations collected in the upper crust. The mesh is  $1 \times 1 \times 0.3$  km (Fig. 5) and it considers (for a selected set of simulations) a single one extensional fault, with Apenninic direction, bordering the NE side of the Larderello field (Fig. 1). The reason for including a single regional deep fault was twofold: firstly to locally simulate the fault contribution to the vertical heat transfer mechanism, connecting the deep heat source (corresponding to the basement rocks) to the over-pressurized reservoirs located between the K horizons, and secondly to study the topologic relationship between the location of the fault and the development and position of the upward and downward rims of the hydrothermal circulation cells (Kühn et al. 2006a).

The boundary conditions include a constant  $T$  ( $20^\circ\text{C}$ ) and a constant hydraulic head (0.1 MPa) at the upper boundary of the model, located at +350 m a.s.l. Zero horizontal gradients of  $T$  and hydraulic head were set on the lateral faces (adiabatic and impermeable boundaries) and

**Fig. 5** 3-D grid ( $42 \times 26 \times 10$  km) of the Larderello numerical model (see location in Figs. 1, 2, 3). View point is from S. the geometry of K-(upper) and  $K_2$  (lower) horizons is shown. The mesh ends in correspondence of the CROP 18A section

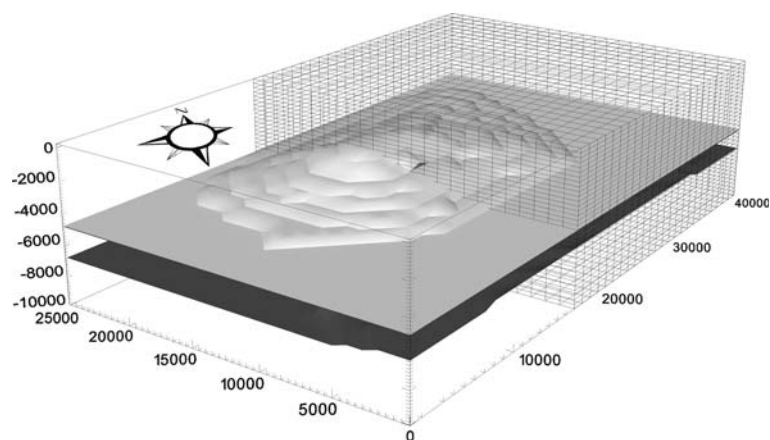


**Table 1** Summary of the boundary conditions for all model simulations

Boundary	Temperature	Head
Top	$T = \text{const.} = 20^\circ\text{C}$	$h = \text{const.}$
Bottom	$T = \text{const.}(400\text{--}600^\circ\text{C})$	$\nabla \times h = 0$
Lateral	$\nabla \times T = 0$	$\nabla \times h = 0$

constant  $T$  and impermeability condition ( $dh/dz = 0$ ) at the bottom boundary. The industrial exploitation of the geothermal fields (steam extraction and water re-injection) was not considered, because of the long time of the simulations (8–12 Ma). The boundary conditions are summarized in Table 1.

Initial values for the thermal properties were assigned according to Bellani and Della Vedova (2004) and Touloukian et al. (1981). The initial conditions include both the geothermal gradient and the gradient of the fluid pressures (when advection/convection is involved). We set an initial linear  $T$  gradient between the upper and the lower boundary. The hydraulic gradient of the fluids was assumed hydrostatic. The  $T$  and pressure effects on fluid density were considered during the simulations.

Our thermal modelling included initial sensitivity studies using variations in the assumed material properties of model components, the most important being the hydrogeologic parameters (such as porosity, permeability and hydraulic head) and the thermal parameters (such as the thermal conductivity and the bottom  $T$  condition).

Table 2 shows the results of the sensitivity analyses on the computed  $T$  distribution, upon changes of the formation thermal conductivity  $\lambda$  of the three main units: changing  $\lambda$  by 20% in the reservoir and basement units (where convection prevails) causes a negligible variation in the  $T$  distribution with depth, vice versa, changing  $\lambda$  by the same amount in the cap rock formations (where conduction prevails) causes a significant change in the  $T$  distribution. The latter change is of the same magnitude as that produced by a  $\lambda$  variation of 20% in all three units.

The results of the sensitivity analysis on the assumed formation porosity (Table 3) are in agreement with those of

**Table 2** Sensitivity analysis of the changes (%) on the average computed  $T$  gradient caused by changes (%) in the average formation thermal conductivity ( $\lambda$ ) of the various units

Domains interested by $\lambda$ change	$\lambda$ change (%)	$T$ gradient change (%)
All three units	+20	−9.5
Reservoir and basement units	+20	+0.6
Cap rock unit	+20	−9.0

Kühn et al. (2006b). For porosity values changing between 0.01 and 0.20 there is very little influence on the  $T$  distribution and flow field pattern (the convective cells remain practically identical), and with the only difference being the simulation time to steady state.

The criteria for deciding the reliability of model results is how well the models match a composite target function, defined by different sets of experimental data, such as: borehole data ( $T$  measurements, geological and geochemical data, fluid inclusion studies) and regional geological and geophysical data (described in the previous chapters).

Because of the inherent uncertainty of many model parameters (e.g., subsurface geometry and properties of the host rocks) and of the initial and boundary conditions (e.g., bottom  $T$ ), a large number of model calculations were run in order to study the range of possible solutions. In this study emphasis was placed on the basal heat flux input (bottom  $T$ ) and on the formation permeability contrast among the three main layers.

We computed more than one hundred models, considering different geometries and boundary conditions and also including the presence of a major regional fault hydraulically connecting the heat input, through the base of the model, with the geothermal reservoirs beneath the upper K-horizon. The latter case was simulated using different contrasts in formation permeability, between the fault and the surrounding rocks. We discuss here the most significant results of the numerical modelling.

**Table 3** Thermal and hydraulic properties of the modelled materials: effective porosity ( $n_e$ ), formation permeability ( $k$ ) heat capacity ( $C$ ) and thermal conductivity ( $\lambda$ )

	Cap rock	Reservoir	Basement	Deep fault	Water
$n_e$ (/)	0.15	0.05	0.03	0.10	/
$k$ ( $\text{m}^2$ )	$10^{-17}$	$5 \times 10^{-15}$ – $5 \times 10^{-16}$	$5 \times 10^{-16}$ – $5 \times 10^{-17}$	$10^{-13}$ – $10^{-14}$	/
$C$ [ $\text{MJ}/(\text{m}^3 \text{K})$ ]	2.18	2.18	2.18	2.18	4.186
$\lambda$ [ $\text{W}/(\text{m K})$ ]	2.5	2.9	2.9	2.9	0.65

$C$  and  $\lambda$  values are matrix values, referred to room  $T$  and pressure conditions

## Crustal stratigraphy and properties of rocks

The upper 10 km of the crust were simply subdivided in the following three main units (Figs. 4, 5), characterized by specific thermal and hydraulic properties (Tables 3, 4):

- *Sedimentary cap rocks.* This layer (3–5 km thick) represents the heterogeneous geological sequences above the upper K-horizon. It is mainly composed by sedimentary rocks (Paleozoic to Present), with limited amount of igneous and metamorphic rocks. The upper boundary of this layer was approximated by the average elevation of about +350 m, characterized by a constant hydraulic head (to avoid the complications of the unsaturated zone). Its bottom is described by the depth to the K-horizon (Accaino et al. 2005, 2006). The permeability of this unit was assumed to be quite low ( $k = 10^{-17} \text{ m}^2$ ) in all models (Table 3) to suppress regional groundwater movement and convective flow, as suggested by the experimental geotherms, which indicate a heat transfer mechanism mainly provided by conduction. This condition is obviously not completely true, because there are several leakage zones in the cap rock, feeding the exploited shallow geothermal reservoirs. Our numerical grid is too coarse ( $1 \times 1 \times 0.3 \text{ km}$ ) to consider these local features and, therefore, the assumed porosity and formation permeability cannot be directly compared with those obtained from experimental flow and pressure well tests in the exploited geothermal wells.
- *Geological sequences between the K horizons.* This layer (1–4 km thick) mainly represents a sequence of metamorphic and intrusive rocks. The upper boundary corresponds to the K-horizon, which was reconstructed as a dome, on the basis of the seismic data. This discontinuity represents a significant change in porosity and fluid content of the formation, locally characterized by over pressured fluids (Accaino et al. 2005). This layer represents the major and regional deep reservoir system

in the Tuscan area, likely fed by deep fluid and mass injections, through the complex and numerous deformation zones (faults, vertical conduits, shear zones).

- *Basement rocks.* This layer (3–4 km thick) mainly represents crystalline basement rocks, locally intruded by dikes and sills, bounded between  $K_2$  and the model total depth (10 km). The hydraulic properties ( $k$  and  $n_c$ ) of this unit are unknown, therefore they were numerically estimated a posteriori in an iterative way, matching a composite target function, defined on the basis of the  $T$  data in the above 3–4 km, the earthquake hypocentral distribution (Vanorio et al. 2004) and the Curie  $T$  depth (Della Vedova et al. 1991).

## Results and discussion

Selected results of 3-D simulations are presented in Figs. 6, 7, 8 and 9. In these examples we evaluate the  $T$  distribution and the fluid flow vectors along the plane including part of the CROP 18A section (Figs. 6, 7) and along a fault plane sub-parallel to the CROP 18A and located to the NE (Fig. 8). Figure 9 is a constant depth view of the same model as in Fig. 6.

The most relevant thermal differences among the various models are produced by changing the permeability value of the “basement layer” and by the change in the bottom  $T$  condition. These parameters are the real variables of the problem. The presence of the vertical fault (Fig. 8) adds a further complication to the model, useful to evaluate the extent, time scale and the effects of the presence of a vertical preferential fluid pathway on the  $T(z)$  distribution.

The simulation time to steady state was variable, depending upon the assumed parameters, from a few Ma (about 5) for the high permeability models (including the fault models), to 10–12 Ma for the low permeability ones. The maximum values of the average linear velocities range

**Fig. 6** 3-D model results computed with model 500\_d parameters (Table 4), simulation time 12 Ma. The SW face shows the CROP 18A section. Different colours indicate  $T$  values; the size of the arrows is proportional to the average linear fluid velocity vectors. Max average linear velocity:  $0.1 \text{ m a}^{-1}$ . See text for more explanation

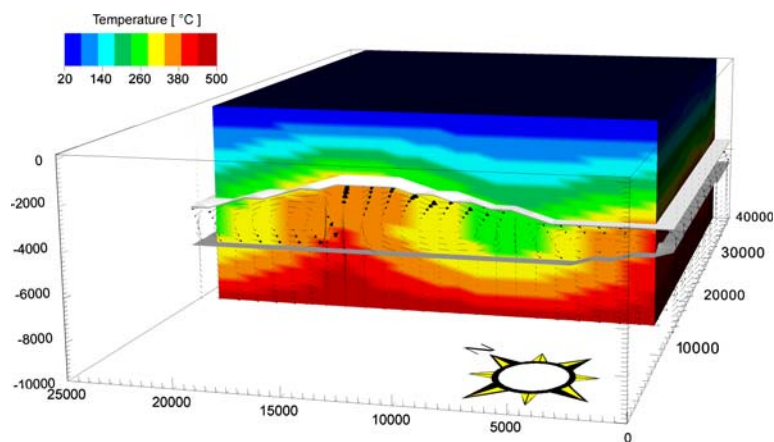


**Fig. 7** 3-D model results computed with model 450\_d parameters (Table 4), simulation time 12 Ma. Part of CROP 18A section is shown to allow the 3-D view of the geometries and  $T$  distribution. The different colours indicate  $T$  values; the size of the arrows is proportional to the average linear fluid velocity vectors. Max average linear velocity:  $<0.1 \text{ m a}^{-1}$ . See text for more explanation

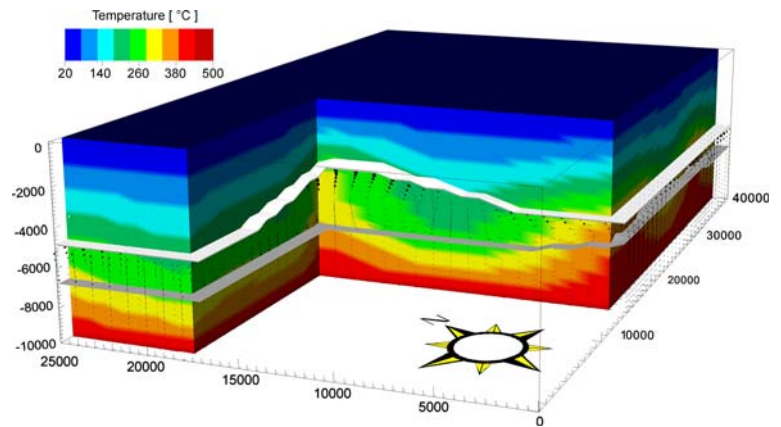


**Fig. 8** 3-D model results computed with model 500\_d parameters (Table 4), including the fault zone to the NE end of the box (Fig. 1). The fault plane is seen from NE, fault permeability  $k = 10^{-13} \text{ m}^2$ , simulation time 8 Ma. The different colours indicate  $T$  values; the size of the arrows is proportional to the average linear fluid velocity vectors. Max average linear velocity:  $0.5 \text{ m a}^{-1}$ . See text for more explanation

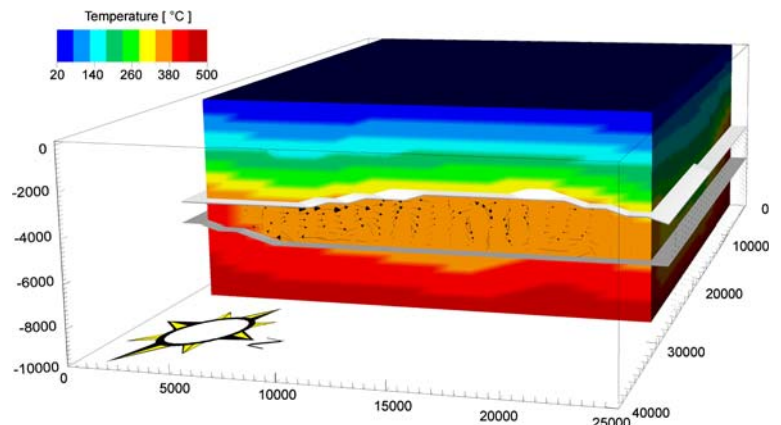
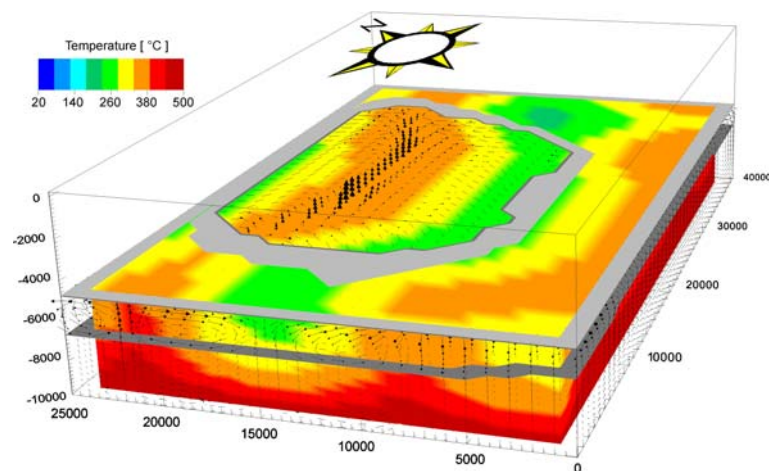


**Fig. 9** 3-D model results at 5 km constant depth, computed with model 500\_d parameters (Table 4), simulation time 12 Ma. View from S. The intersection with the K-horizon is artificially enlarged (gray closed band). The size of the arrows is proportional to the average linear fluid velocity vectors. Max average linear velocity:  $0.1 \text{ m a}^{-1}$ . See text for more explanation



from  $1.5 \times 10^{-8}$  (about  $0.5 \text{ m a}^{-1}$ ) to  $3.1 \times 10^{-9} \text{ m s}^{-1}$  ( $0.1 \text{ m a}^{-1}$ ) for the high and low permeability reservoirs, respectively.

#### Parameters calibration

The formation permeability  $k$  and the thermal conductivity  $\lambda$  (Table 3) were, particularly, subject to calibration, by

minimizing the residual between computed and observed  $T$ - $z$  data.

The estimate of the rock and fluid parameters strongly depends on the assumed petrogenetic model. Using variations in the assumed material properties we conducted sensitivity studies on the propagation of uncertainties in the input parameters, downstream to the thermal modelling results. For this purpose, we created several sets of models to calibrate the formation permeability and the bottom  $T$ .

**Table 4** Index map of the formation permeability ( $k$ ) for the model subscripts a, b, c, d, with a bottom  $T$  of 500°C

Model ID	Formation permeability ( $k$ )					
	Cap rock unit		Reservoir unit		Basement unit	
	m <sup>2</sup>	mDarcy	m <sup>2</sup>	mDarcy	m <sup>2</sup>	mDarcy
500_a	10 <sup>-17</sup>	0.01	5 × 10 <sup>-15</sup>	5	5 × 10 <sup>-16</sup>	0.5
500_b	10 <sup>-17</sup>	0.01	5 × 10 <sup>-16</sup>	0.5	5 × 10 <sup>-16</sup>	0.5
500_c	10 <sup>-17</sup>	0.01	5 × 10 <sup>-15</sup>	5	5 × 10 <sup>-17</sup>	0.05
500_d	10 <sup>-17</sup>	0.01	5 × 10 <sup>-16</sup>	0.5	5 × 10 <sup>-17</sup>	0.05

Table 4 summarizes the formation permeability assumptions for one set of these models, with bottom  $T$  of 500°C.

Further sets of models were run using the formation permeability contrasts of Table 4, but assuming a different bottom  $T$  boundary condition, every 50°C, from 400 to 600°C. The reason for choosing 400°C as the lower  $T$  limit is because it cannot be cooler than the  $T$  observed in the Carboli 11 well (437°C at 3,343 m depth, see well location in Fig. 13), on the other hand the upper  $T$  limit (600°C) approximately corresponds to the Curie  $T$ , estimated at about 10 km depth.

In all simulations the computed  $T$  was monitored against the target function, at two reference sites: RS1 in the centre of the Larderello geothermal field and RS2, located 10–12 km to the east, in between the Larderello and Travale fields (Fig. 13). The experimental  $T$ - $z$  distribution in the

areas surrounding RS1 (within a square box approximately 10 × 10 km) and RS2 (within a square box approximately 5 × 5 km) have been used for comparison with the computed geotherms  $T(z)$ , as shown in Figs. 10, 11 and 12. By minimizing the residuals between computed and observed  $T$ - $z$  data we estimated the best average values for the bottom  $T$  and for the permeability contrast between the two deeper layers (Table 4). Among all the simulations (Figs. 10–12), the ones with 500 ± 50°C bottom  $T$  condition provided the best matching with the observations.

We also checked the simulations with respect to two different scenarios, i.e.: considering an average constant permeability of the reservoir rocks between  $K_1$  and  $K_2$  horizons (Figs. 6, 7), and assuming a localized vertical fault zone with NW–SE direction, bordering to the NE the Larderello field (Fig. 8). Therefore, there will be two

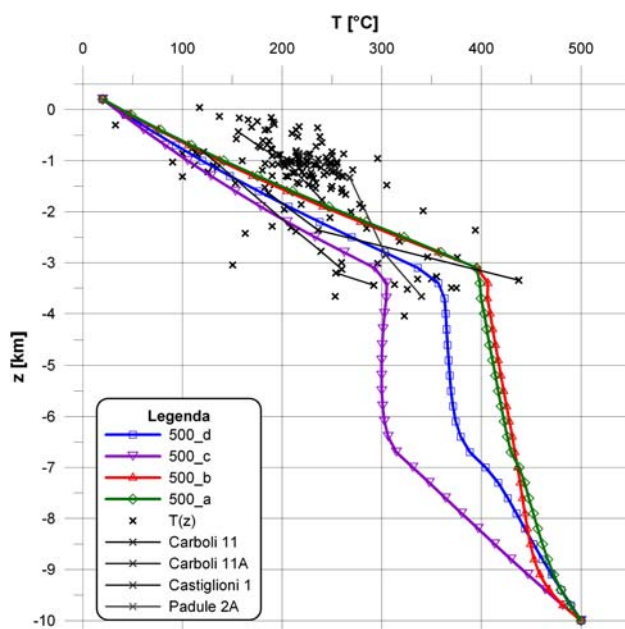


**Fig. 10** Computed geotherms  $T(z)$  versus bottom hole experimental  $T$ - $z$  and a few selected multipoint geotherms single wells in the RS1 target area (position in Fig. 13). The four geotherms from the surface down to 10 km depth where computed with the model parameters as in Table 4. Bottom  $T = 500^\circ\text{C}$

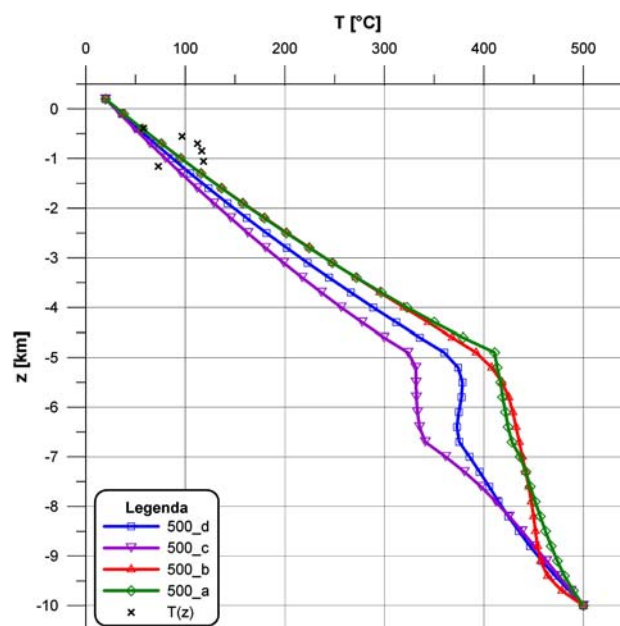


**Fig. 11** Computed geotherms  $T(z)$  versus a few experimental  $T$ - $z$ , off the Larderello field (see RS2 position in Fig. 13). The four geotherms from the surface down to 10 km depth were computed with the model parameters as in Table 4. Bottom  $T = 500^\circ\text{C}$

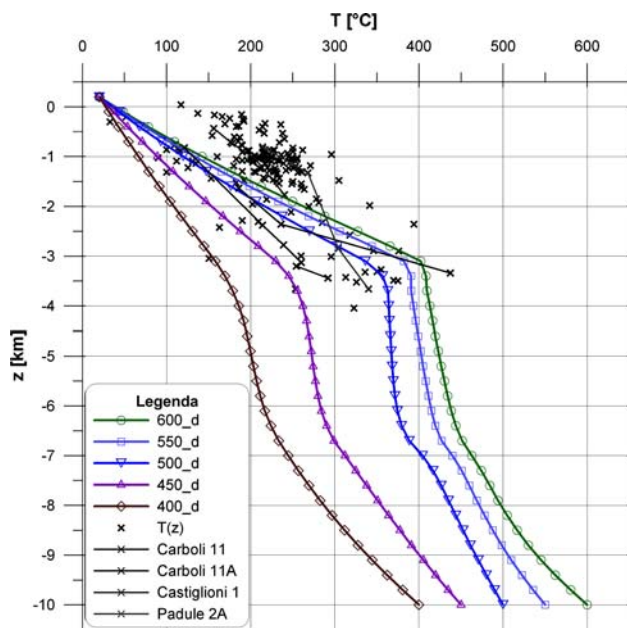
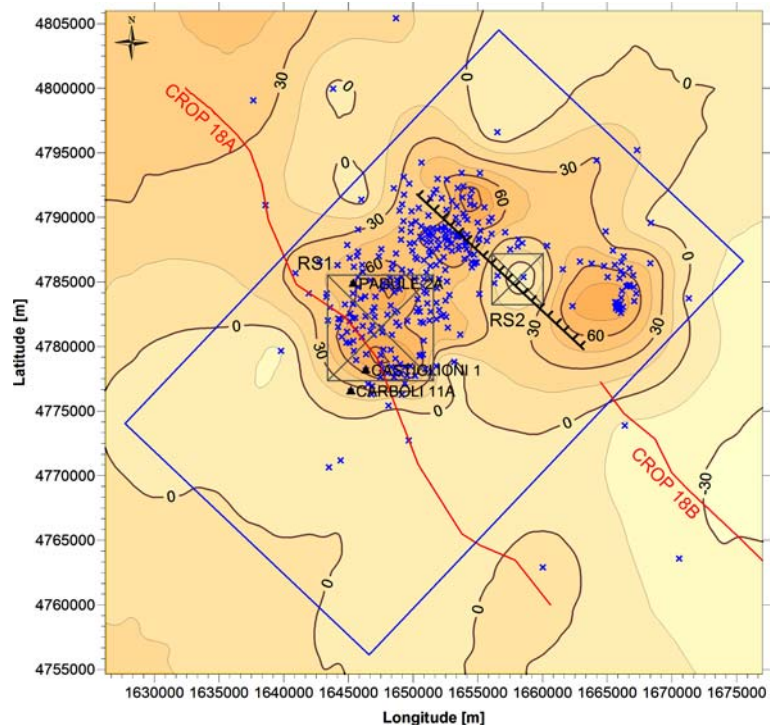


**Fig. 12** Computed geotherms versus both experimental  $T$ - $z$  and a few selected measured geotherms within the RS1 area (position in Fig. 13) in the Larderello geothermal field, simulated with variable bottom  $T$  conditions (every 50°C, from 400 to 600°C). The five geotherms from the surface down to 10 km depth were computed with the model parameters 500\_d, as in Table 4

further sets of simulations to compare with each reference site.

The difference between the observed geothermal gradient at 1,000 m depth and the computed gradient at the

**Fig. 13** Smoothed  $T$  gradient residuals ( $T$  experimental- $T$  computed) in the upper 1 km of sediment. The simulation parameters for the computed  $T$  gradient are those of model 500\_d (Table 4), with fault permeability  $k = 10^{-13} \text{ m}^2$ . Location of selected wells with observed geotherms (Figs. 10, 12) is shown (black triangles). Blue crosses are geothermal boreholes with single  $T$  measurements. Target sites (RS1 and RS2) and the fault location are also indicated



same depth was also produced (Fig. 13), to evaluate the 3-D distribution of the geothermal field.

Additional data for model calibration come were provided by interpreted CROP profiles (presence of over pressured fluids), geochemistry data (He isotopes and isotope ratios), fluid inclusion data (trapping  $T$ ) and gravity data (lateral heterogeneity in mass distribution at selected depths).

Simulations without considering the presence of the fault

The conditions for the simulations shown in Fig. 6 (Model 500\_d) and Fig. 7 (Model 450\_d) are very similar, differing in the bottom  $T$  condition only. The 3-D  $T$  and velocity fields show as the  $T$  and pressure structures of the Larderello field are driven by geometry, formation permeability, permeability contrasts among the main layers, and by heat input from below. It is possible to recognize two clear large convective cells in the reservoir between K horizons, along the CROP 18A section, oriented from NW (left hand side) to SE, and a third smaller cell to the SE end (Fig. 6). The size of the velocity vectors is proportional to the average linear velocity. The vertical plane through the culmination of the K-horizon (orthogonal to the page) corresponds to the deep “aquifer divider”, being the locus of an upward diverging flow of two large adjacent convective cells. The descending rim of the SE

convective cell contributes to the cooling (green colour) within the reservoir. The simulated  $T$  for the upward fluid circulation is of the order of 400°C (Fig. 6), for a bottom  $T$  condition of 500°C, and of the order of 300°C, for a bottom  $T$  condition of 450°C (Fig. 7). The former values allow a better matching between simulated and measured  $T$ , at about 3–4 km depth in the Larderello field (Fig. 10.) The lateral extent of the anomalous  $T$  in the reservoir rocks, sustained by the ascending geothermal fluids, is of the order of 7–8 km, for the conditions simulated in Fig. 6, and it corresponds to the area interested by over-pressurized fluids on the interpreted seismic section of CROP 18A (Fig. 4). Moreover, this distance is of the same order of magnitude of the lateral extension (about 10 km) of the observed thermal gradient anomaly (Fig. 2) and of the  $^3\text{He}/^4\text{He}$  isotopic anomaly at the surface (Magro et al. 2003). Furthermore, the conditions simulated in Fig. 7 do not match either the observed  $T$  values at 3–4 km depth (Fig. 10), or the wavelength of the observed positive geothermal gradient anomaly (Fig. 2). The comparison between the two simulations shows as the bottom boundary  $T$  condition is extremely critical with respect to the simulated  $T$  and fluid velocity fields in the 3-D domain, although the convective cells have the same position, extent and circulation sense.

Given the low assumed permeability for the upper cap rock layer, the fluid velocity and  $T$  field in the model domain is driven by the permeability contrast between basement layer and reservoir layer and by the bottom  $T$  condition.

The horizontal section of 500\_d model (Fig. 9) intersects the K-horizon at 5 km depth, allowing to reconstruct the space distribution of the convective cells. Three main convective cells extending in a sinuous way all along the longitudinal side of the model (with a NE–SW direction) can be recognized: the two adjacent ones interesting the Larderello field contribute to an upward converging flow, sustaining a strong advective vertical heat transfer (orange), whereas the two cells to the SE sustain a downward flow, characterized by a negative  $T$  anomaly (green). The geometry and boundary conditions of the models strongly influence the solutions close to the borders; nonetheless the central part of the simulated domain provides results in good agreement with the available observations within the calibration target sites (RS1 and RS2 in Fig. 13). The computed 1-D geotherms for the Larderello field are compared in Fig. 10 with the available experimental measurements, assuming a bottom  $T$  value condition of 500°C and four different permeability contrast (as shown in Table 4). The  $T$  measurements and thermal gradients measured within the upper layer are not adequately described by model simulations, both as absolute  $T$  values and as thermal gradients. There are two main

reasons for this: first, because we wanted to extract the low frequency signature of the main regional geotherms (suggesting a prevailing heat transfer by conduction), thus avoiding the local effects due to lithology and structural heterogeneities, second, because the formation permeability of the cap rock is qualitatively bimodal: very high in correspondence of the localized fresh fractures and faults and very low in correspondence of the bulky rock.

To understand the meaning of the four different geotherms (labelled 500\_a, 500\_b, 500\_c, and 500\_d, according to the formation permeability values listed in Table 4 below the K-horizon depth (Fig. 10), it is useful to analyze them in three steps: first comparing 500\_a with 500\_c geotherms, then comparing 500\_b with 500\_d and finally cross-correlating the two groups together. However, it should be noticed that the simulated geotherms represent the  $T(z)$  distribution in a vertical column of cells with a base area of  $1 \times 1$  km, whereas the experimental data refer to larger target areas of  $10 \times 10$  km (RS1) and  $5 \times 5$  km (RS2), respectively.

The first group compares the simulation results between two models with the same formation permeability in the reservoir (5 mDarcy) and in the cap rock (0.01 mDarcy) layers, respectively, differing by the permeability of the basement layer only. The two geotherms are very different, with the 500\_c geotherm strongly two-legged below the K-horizon. Thus the formation permeability of the basement layer appears to be the most critical parameter in controlling the mass and energy transport toward the upper levels, and, as a consequence, the  $T$  distribution within the modelled domain.

The other two models (500\_b and 500\_d) have the same formation permeability in the reservoir layer (0.5 mDarcy), but these values are one order of magnitude lower with respect to the first two models. The 500\_b model has a single homogeneous deep unit (reservoir + basement) with the same formation permeability. The two geotherms are much closer, but show an analogous behaviour as the previous ones. Also in this case, the permeability of the bottom basement layer drives the mass and energy flow entering the domain from the bottom boundary.

The above comparisons suggest that the shape of the geotherms (almost linear versus two-legged) in the two deeper layers is controlled by the formation permeability of the basement layer, with almost linear geotherms in the case of high permeability of the bottom layer. In this case, the change in formation permeability of the reservoir rocks produces slight changes between the 500\_a and 500\_b geotherms. Because of the  $T$  boundary condition and the homogeneous permeability of the 500\_b model, the average thermal gradient between 3.5 and 9 km is almost constant (apart from the lower boundary condition).

On the other hand, when the formation permeability of the bottom layer is very low (models 500\_c and 500\_d), the two-legged geotherms could spread over a larger domain of the  $T$ - $z$  space, as a function of the formation permeability of the above reservoir rocks. If the hydraulic resistance of the reservoir is lower, then the total mass and energy fluxes through it is higher, with higher  $T$  gradients in the basement unit and very low  $T$  gradients in the reservoir unit; vice versa, if the hydraulic resistance of the reservoir is higher (model 500\_d), then the  $T$  gradients in the basement unit are lower and the  $T$  gradients in the reservoir unit are higher, with respect to the corresponding gradients of the 500\_c model. The highest  $T$  value, measured at about 3.2 km depth in the Carboli 11 well (Barelli et al. 2000) is anomalously high, corresponding to simulated  $T$  at depths greater than about 6 km. This measurement was conservatively assumed to correspond to vertical mass/heat input from greater depths. The lateral  $T$  variability at about 3.5 km depth beneath the Larderello field is enormous, ranging between 250 and 440°C (average of about 350°C), suggesting that the field is still far from thermal equilibrium.

Figure 11 shows the same geotherms as in Fig. 10, but for the NE marginal area of the Larderello geothermal field (RS2 in Fig. 13). In this case the comparison between simulations and experimental data is not very informative, because of the lack of deep information in areas less interesting from the exploitation point of view. Nonetheless, the interpretation of these geotherms is expected to follow the same line of reasoning as for the geotherms in Fig. 10.

The geotherm 500\_d in Fig. 10 was assumed to correspond to an average  $T$  distribution with depth for the field, therefore the formation permeability values used for that simulation (Table 4) were chosen to run several simulations with changing bottom  $T$  boundary condition, with the aim of evaluating its effect on the computed geotherms (Fig. 12). We assumed five different bottom  $T$  values, every 50°C, in the  $T$  interval from 400 to 600°C and compared the resulting geotherms with available  $T$ - $z$  measurements. The geotherms better constraining the observations require a bottom  $T$  of at least  $500 \pm 50^\circ\text{C}$ .

The comparison between observed and computed  $T$ -gradients (using model 500\_d with fault) in the upper 1 km is shown in Fig. 13 as residuals map. Computed and observed anomalies are in reasonable good agreement for the regional field, whereas, at shorter wavelength, there are three main discrepancies, with differences up to  $60 \text{ mK m}^{-1}$ . These large residuals correspond to the local high intensity thermal gradient anomalies, generated by the shallow exploited reservoirs, which were not included in our simulations. The location of wells with a single  $T$  value (blue crosses) and with multiple  $T$  measurements (black triangles) are also shown (see also Figs. 10–12).

## Simulations with the presence of the fault

The extensional fault zone with Apenninic direction (Fig. 1) was simulated as a vertical prism, completely internal to the model domain, in order both to avoid singularities at the boundaries and to consider the likely ductile behaviour of the rocks from the  $K_2$  horizon down to the model bottom. Therefore, the fault extends from about 7 km depth up to the K-horizon (located at about 4.6 km depth), or even higher (2.2 km depth into the cap rock) in other simulations. The fault is 1 km thick and characterized by a formation permeability ranging from 10 to 100 mDarcy.

The simulation results show how the depth to the top of the fault zone is critical for the development, or absence of the shallow geothermal reservoirs. The thermal gradients away from the fault, and particularly above its top, might be very high, depending upon the permeability contrast between the fault and the country rock (with a very low formation permeability) and upon the depth to the fault bottom. Assuming the fault top at 2.2 km, the computed thermal gradients largely exceed the experimental  $T$  gradients in the upper 1 km layer, thus indicating that the fault presence and geometry and/or the assumed formation permeability for the fault are not appropriate. Depths to the fault top greater than 4 km produce  $T$  distributions closer to the measured  $T$  data.

The upward fluid flow through fractures and the associated heat transfer mechanism are likely more adequate in other areas of the Larderello field, where the fractures network operates at a more localized and dense pattern, to sustain the shallow geothermal reservoirs. The simulation with the fault zone interesting the reservoir rocks only (corresponding to a vertical high permeability zone of 100 mDarcy connecting the two K horizons), computed with the formation permeability as the 500\_d model (Table 4), shows the development of several convective cells in the fault zone volume (Fig. 8). The figure shows the fault zone plane, which has a direction sub-parallel to the CROP 18A profile. The velocity vectors of Figs. 6 and 8 have the same scale, allowing the comparison of the velocity field in a homogeneous layer (Fig. 6), with the same field in a fault plane (Fig. 8). In the latter case, the mass and heat transfer from the basement rocks to the top of the reservoir (K-horizon) is substantially enhanced, inducing a higher heat flux through the overlying cap rocks.

The  $T$  and pressure perturbations in the reservoir, away from the fault, are strongly dependent upon the specific geometry and properties chosen for each simulation. Using for the fault zone a formation permeability of 100 mDarcy and the other parameters as in model 500\_d (Table 4), the lateral effects on the  $T$  field within the reservoir, measured at the RS1 and RS2 target sites, are quite different,

depending upon the lateral distance and permeability contrast between the fault zone and the country rocks. However, the comparison between models with and without the fault shows somehow comparable results. The thermal effects in the cap rock layer, because of the presence of a fault confined below the K-horizon, are significant near the fault top, but they fade away rapidly, because of the low permeability of this layer.

## Conclusions

Geological and geophysical data were integrated into a simple 3-D conceptual model, considering heat and mass fluxes from below the K<sub>2</sub> horizon, in order to investigate heat transfer mechanism and the rule of both formation permeability and bottom *T* boundary conditions.

The comparison between observed and computed *T* data was used to highlight the possible variability of the bottom *T* and formation permeability of the two deeper units.

The results indicate the crucial role of the hydraulic resistance contrast within the deeper layers and of the bottom *T* on the upward heat transfer rate.

A few scenarios are coherent with the regional framework:

- predominant thermal convection between K horizons (high *k* with limited over-pressure) and hydraulically resistant bottom layer (models 500\_a, 500\_c);
- limited thermal convection between K horizons (low *k*, i.e., over-pressure) and high *k* values below (i.e., more efficient mass flux from the lower crust an upper mantle, models: 500\_b, 500\_d);
- general “cap rock” behaviour of the formations above K-horizon (apart from local heterogeneities, such as the shallow reservoirs).

The simulations results represent almost steady-state conditions and do not consider neither any change with time of the bottom *T* boundary condition, nor any episodic dike/fluid intrusion into the upper crust layers, as it should be expected, considering the available petrologic (Villa and Puxeddu 1994; Gianelli and Laurenzi 2001) and fluid inclusion data (Magro et al. 2003). Not being able to dimension space, time, mass and heat input of these intrusion events, we conceptually simulated the effects of a single fault disturbance in the above-discussed models, as an analogue to the input of extra heat into the model. The reliability of these models is, therefore, qualitative and generally considered valid for the comprehension of heat transfer mechanisms, at regional scale, but it cannot be used for local scale features.

The borehole *T*(*z*) data, integrated with hypocentral distribution, fluid inclusions studies, isotope geochemistry

and Curie *T* depth suggest a bottom *T* of  $500 \pm 50^\circ\text{C}$  at about 10 km depth (Dini et al. 2005). The rule of *P-T* conditions in high enthalpy geothermal fields is more critical than the geological framework and inherited structural features, although locally tectonics may be important.

The overall evaluation of the model results suggests as the major source of uncertainty pertains to the poorly constrained parameters of heat input and permeability of the reservoir and basement rocks, such as: the space distribution and age of the dike intrusions, their depth of emplacement, the residence time of magma before eruption and the permeability change with time.

**Acknowledgments** We are grateful to several colleagues and friends for constructive criticism and discussion. We thank Prof. Izzy Kutasov and an anonymous reviewer for their constructive criticism and precious comments. This work was partly supported by COFIN-MIUR 2006 funding to the first authors.

## Appendix 1

The numerical modelling was performed using the commercial code SHEMAT 7.1 (Clauser 2003) considering various boundary conditions, inner geometries and formation permeabilities.

SHEMAT 7.1 code (Clauser 2003) was used to carry out the simulations of coupled heat and fluid fluxes. The solute transport was not simulated, although we assumed a purely speculative average density of the fluid of  $1,100 \text{ kg m}^{-3}$  (at room *T*). The 3-D regional conductive-convective model was realized by means of unsteady forward simulations, under the assumptions of impervious and isothermal top and bottom boundaries, lateral adiabatic faces and variable internal physical properties.

Solving the non stationary problem consists of finding the *T*, pressure and fluid velocity fields within the model domain, assuming appropriate initial and boundary conditions.

The code SHEMAT was used to simulate both the solid-state heat conduction and the conductive-convective flow of pore fluids. Non-stationary equations of non-isothermal hydrodynamics, accounting for phase transition, were used to carry out the three dimensional modelling of the convective flow. The most important assumptions were:

- flow conforms to Darcy’s law;
- effects of the capillary pressure are neglected;
- both phases (solid matrix, liquid) are considered to be in local thermal equilibrium;
- fluid flow does not affect the solid matrix.

The problem is described by a system of mass and energy conservation equations in Cartesian coordinates for

convective two-phase flow through a porous medium (Faust and Mercer 1979):

$$\nabla \cdot (\underline{\lambda} \nabla T - \rho_f c_f T \vec{v}) = \frac{\partial T}{\partial t} [n \rho_f c_f + (1-n) \rho_m c_m] \quad (1)$$

$$\underbrace{\rho_f g (\alpha + n \beta)}_{S_S} \frac{\partial h_0}{\partial t} = \nabla \cdot \left[ \underbrace{\frac{\rho_f g k}{\mu}}_{\underline{K}} (\nabla h_0 + \rho_r \nabla z) \right] \quad (2)$$

where

- $\alpha$  rock compressibility (Pa<sup>-1</sup>);
- $\beta$  fluid compressibility (Pa<sup>-1</sup>);
- $c$  specific heat capacity (J kg<sup>-1</sup> K<sup>-1</sup>);
- $g$  gravitational acceleration (m s<sup>-2</sup>);
- $h$  hydraulic potential, head (m);
- $\underline{\lambda}$  tensor of thermal conductivity (W m<sup>-1</sup> K<sup>-1</sup>);
- $\underline{k}$  tensor of permeability (m<sup>2</sup>);
- $\underline{K}$  tensor of hydraulic conductivity (m s<sup>-1</sup>);
- $n$  porosity (/);
- $\rho$  density (kg m<sup>-3</sup>);
- $S_S$  specific storage coefficient (m<sup>-1</sup>);
- $T$  temperature (K);
- $t$  time (s);
- $\vec{v}$  Darcy (filtration) velocity; specific discharge (m s<sup>-1</sup>).

## Subscripts

- $f$  liquid;
- $m$  matrix;
- $0$  reference condition.

SHEMAT assumes the properties of water as a function of fluid pressure and  $T$  for pressure greater than saturation pressure or  $T$  lower than critical  $T$ , limited to pressure and  $T$  below 100 MPa and 1,000°C, respectively (Meyer et al. 1979). SHEMAT accounts for the  $T$  dependence of rock thermal conductivity according to Zoth and Hänel (1988). Examples of the application of the SHEMAT code may be found in Clauser (2003).

## References

- Accaino F, Tinivella U, Rossi G, Nicolich R (2005) Geofluid evidence from analysis of deep crustal seismic data (Southern Tuscany, Italy). *J Volcanol Geotherm Res* 148:46–59
- Accaino F, Nicolich R, Tinivella U (2006) Highlighting the crustal structure of the southern Tuscany by reprocessing the CROP 03 profile. *Boll Geof Teor Appl* 47(3):425–445
- Acocella V, Rossetti F (2002) The role of extensional tectonics at different crustal levels on granite ascent and emplacement: an example from Tuscany (Italy). *Tectonophysics* 354:71–83
- Bailey RC (1990) Trapping of aqueous fluids in the deep crust. *Geophys Res Lett* 17:1129–1132
- Baldi P, Bellani S, Ceccarelli A, Fiordelisi A, Squarci P, Taffi L (1995) Geothermal anomalies and structural features of southern Tuscany. In: *proc world geothermal congress, Florence, Italy vol 2*, pp 693–696
- Baldi P, Bertini G, Ceccarelli A (1993) Geothermal fields of central Italy. *Res Geol* 16:69–81
- Barelli A, Bertini G, Buonasorte G, Cappetti G, Fiordelisi A (2000) Recent deep exploration results at the margins of the Larderello-Travale geothermal system. In: *proc World Geothermal Congress, Kyushu-Tohoku, Japan*, pp 965–970
- Barzaghi R, Betti B, Borghi A, Sona G, Tornatore V (2002) The Italian quasi-geoid ITALGEO99. *Boll Geodesia Scienze Affini* 1:33–51
- Batini F, Burgassi PD, Cameli GM, Nicolich R, Squarci P (1978) Contribution to the study of the deep lithospheric profiles: deep reflecting horizons in Larderello-Travale geothermal field. *Mem Soc Geol It* 19:477–484
- Bellani S, Della Vedova B (2004) 2-D thermal modelling across the geothermal fields of Tuscany, Italy. *Eos Trans, AGU*, 85 (47) Fall Meeting, Abstract T43B–1326
- Bellani S, Brogi A, Lazzarotto A, Liotta D, Ranalli G (2004) Heat flow, deep temperatures and extensional structures in the Larderello Geothermal Field (Italy): constraints on geothermal fluid flow. *J Volcanol Geotherm Res* 132:15–29
- Bellani S, Magro G, Brogi A, Lazzarotto A, Liotta D (2005) Insights into the Larderello geothermal field: structural setting and distribution of thermal and <sup>3</sup>He anomaly. In: *proc World Geothermal Congress, Antalya, Turkey*, pp 1–4
- Brogi A, Lazzarotto A, Liotta D, Ranalli G (2003) Extensional shear zones as imaged by reflection seismic lines: The Larderello geothermal field (central Italy). *Tectonophysics* 363:127–139
- Brogi A, Lazzarotto A, Liotta D, Ranalli D, CROP–18 Working Group (2005) Crustal structures in the geothermal areas of southern Tuscany (Italy): insights from CROP-18 deep seismic reflections lines. *J Volcanol Geotherm Res* 148:60–80
- Brunet C, Monié P, Jolivet L, Cadet JP (2000) Migration of compression and extension in the Tyrrhenian Sea, insights from 40Ar/39Ar ages on micas along a transect from Corsica to Tuscany. *Tectonophysics* 321:127–155
- Carmignani L, Decandia FA, Fantozzi PL, Lazzarotto A, Liotta D, Meccheri M (1994) Tertiary extensional tectonics in Tuscany (Northern Apennines, Italy). *Tectonophysics* 238:295–315
- Carmignani L, Lazzarotto A, Brogi A, Conti P, Cornamusini G, Costantini A, Meccheri M, Sandrelli P (2004) Carta geologica della Toscana. Regione Toscana, Direzione Generale delle Politiche Territoriali e Ambientali, Servizio Geologico
- Clauser C (2003) Numerical simulation of reactive flow in hot aquifers. SHEMAT and Processing SHEMAT. Springer, Berlin, pp 1–333
- Decandia FA, Lazzarotto A, Liotta D, Cernobori L, Nicolich R (1998) The CROP 03 traverse: insights on post-collisional evolution of northern Apennines. *Mem Soc Geol It* 52:427–439
- Della Vedova B, Marson I, Panza GF, Suhadolc P (1991) Upper mantle properties of the Tuscan-Tyrrhenian area: a key for understanding the recent tectonic evolution of the Italian region. *Tectonophysics* 195:311–318
- Della Vedova B, Bellani S, Pellis G, Squarci P (2001) Deep temperatures and surface heat flow distribution. In: Vai GB, Martini IP (eds) *Anatomy of an orogen: the Apennines and adjacent Mediterranean basins*. Kluwer, Dordrecht, pp 65–76

- Dini A, Gianelli G, Puxeddu M, Ruggieri G (2005) Origin and evolution of Pliocene-Pleistocene granites from the Larderello geothermal field (Tuscan Magmatic Province, Italy). *Lithos* 81:1–31
- Faust CR, Mercer JW (1979) Geothermal reservoir simulation 1. Mathematical models for liquid and vapor-dominated hydrothermal systems. *Water Resour Res* 15(1):23–30
- Fournier RO (1991) The transition from hydrostatic to greater than hydrostatic fluid pressures in presently active continental hydrothermal systems in crystalline rock. *Geophys Res Lett* 18:955–958
- Ghisetti F, Vezzani L (2002) Normal faulting, transcrustal permeability and seismogenesis in the Apennines (Italy). *Tectonophysics* 348:155–168
- Gianelli G, Laurenzi MA (2001) Age and cooling rate of the geothermal system of Larderello. *Geotherm Res Counc Trans* 25:731–735
- Giese P, Wigger P, Morelli C, Nicolich R (1981) Seismische studien zur bestimmung der krustenstruktur-anomalien der Toskana. Commission European Communities, EUR, pp 1–108
- Kennedy BM, Kharaka YK, Evans WC, Ellwood A, DePaolo DJ, Thordsen J, Ambats G, Mariner RH (1997) Mantle fluids in the San Andreas fault system, California. *Science* 278:1278–1281
- Kennedy BM, Van Soest MC (2006) A helium isotope perspective on the Dixie Valley, Nevada hydrothermal system. *Geothermics* 35–1:26–43
- Kühn M, Zeeb C, Gessner K (2006a) 2D or not 2D: are two dimensions enough to accurately model convective fluid flow through faults and surrounding host rocks? In: *proc computational methods in water resources—XVI*, Copenhagen, Denmark, pp 1–8
- Kühn M, Dobert F, Gessner K (2006b) Numerical investigation of the effect of heterogeneous permeability distributions on free convection in the hydrothermal system at Mount Isa, Australia. *Earth Planet Sci Lett* 244:655–671
- Liotta D, Ranalli G (1999) Correlation between seismic reflectivity and rheology in extended lithosphere: Southern Tuscany, inner northern Apennines, Italy. *Tectonophysics* 315:109–122
- Liotta D, Cernobori L, Nicolich R (1998) Restricted rifting and its consistence with compressional structures: Results From Crop-3 Traverse (Northern Apennines, Italy). *Terra Nova* 10(1):16–20
- Locardi E, Nicolich R (2005) Crust-mantle structures and Neogene-Quaternary magmatism in Italy *Boll Geof Teor Appl* 46(2–3):169–180
- Magro G, Ruggieri G, Gianelli G, Bellani S, Scandiffio G (2003) Helium isotopes in paleofluids and present-day fluids of the Larderello geothermal field: constraints on the heat source. *J Geophys Res* 108-B1:1–12
- Marinelli G, Barberi F, Cioni R (1993) Sollevamenti Neogenici ed intrusioni acide della Toscana e del Lazio settentrionale. *Mem Soc Geol It* 49:279–288
- Marson I, Cernobori L, Nicolich R, Stoka M, Liotta D, Palmieri F, Velicogna I (1998) CROP03 profile: a geophysical analysis of data and results. *Mem Soc Geol It* 52:123–137
- Mattei M, Kissel C, Funicicchio R (1996) No tectonic rotation of the Tuscan Tyrrhenian margin (Italy) since late Messinian. *J Geophys Res* 101:2835–2845
- Meyer CA, McClintock RB, Silvestri GJ, Spencer RC (1979) ASME steam table—thermodynamic and transport properties of steam. American Society of Mechanical Engineers, New York
- Mongelli F, Puxeddu M, Zito G (1989) Anomalie residue del flusso di calore nella fascia toscano-laziale: interpretazione della anomalia di Larderello. In: *proc VIII Conference “Gruppo Nazionale Geofisica della Terra Solida”*, Rome, pp 1147–1170
- Nicolich R (1989) Crustal structures from seismic studies in the frame of the European Geotraverse (southern segment) and CROP projects. In: Boriani A, Bonafede M, Piccardo GB, Vai GB (eds). *The lithosphere in Italy: advances in earth science research*. Accademia Nazionale dei Lincei, Roma pp 41–61
- Nicolich R, Marson I (1994) Caratteri geofisici delle strutture crostali nella Provincia Geotermica Toscana. *Studi Geologici Camerti* 1:163–168
- Panza GF, Pontevivo A, Chimera G, Raykova R, Aoudia A (2003) The lithosphere-asthenosphere: Italy and surroundings. *Episodes* 26:169–174
- Pascucci V, Merlini S, Martini IP (1999) Seismic stratigraphy of the Miocene–Pleistocene sedimentary basins of the northern Tyrrhenian sea and western Tuscany (Italy). *Basin Res* 11:337–356
- Piomallo C, Morelli A (1998) P-wave propagation heterogeneity and earthquake location in the Mediterranean region. *Geophys J Int* 135:232–254
- Scrocca D, Doglioni C, Innocenti F, Manetti P, Mazzotti A, Bertelli L, Burbi L, D’Offizi S (eds) (2003) CROP ATLAS—Seismic Reflection Profiles of the Italian Crust. *Memorie Descrittive della Carta Geologica d’Italia*, vol LXII, Dipartimento Difesa del Suolo, APAT, Roma, pp 1–194
- Serri G, Innocenti F, Manetti P (1993) Geochemical and petrological evidence of the subduction and delaminated Adriatic continental lithosphere in the genesis of Neogene–Quaternary magmatism of central Italy. *Tectonophysics* 223:117–147
- Sinigoi S, Quick JE, Peressini G, Mayer A (2003) An example of the Apulian lower crust: the Ivrea-Verbano zone. *Transalpine conference ext. abs. of oral and poster presentations*. *Mem Sci Geol* 54:101–104
- Spakman W (1990) Tomographic images of the upper mantle below central Europe and the Mediterranean. *Terra Nova* 2:542–553
- Straus JM, Schubert G (1977) Thermal convection of water in a porous media: effects of temperature- and pressure-dependent thermodynamics and transport properties. *J Geophys Res* 82:325–333
- Tinivella U, Accaino F, Rossi G, Nicolich R (2005) Petrophysical analysis of CROP-18 crustal seismic data. *Boll Soc Geol It* 3:205–211
- Touloukian YS, Judd WR, Roy RF (eds) (1981) Physical properties of rocks and minerals. MacGraw Hill/CINDAS data series on material properties vol II-2 Purdue Research Foundation, pp 1:549
- Vanorio T, De Matteis R, Zollo A, Batini F, Fiordelisi A, Ciulli B (2004) The deep structure of the Larderello-Travale geothermal field from 3D microearthquake traveltime tomography. *Geophys Res Lett* 31: L07613, DOI: [10.1029/2004GL019432](https://doi.org/10.1029/2004GL019432)
- Velicogna I, Marson I, Suhadolc P (1996) Morfologia della Moho da gravità, topografia ed isostasia. In: *proc XIV conference “Gruppo Nazionale Geofisica della Terra Solida”* Roma vol 1, pp 405–418
- Villa I, Puxeddu M (1994) Geochronology of the Larderello geothermal field: New data and the “closure temperature” issue. *Contrib Mineral Petrol* 115:415–426
- Zoth G, Hänel R (1988) Appendix. In: Hänel R, Rybach L, Stegena L (eds) *Handbook of terrestrial heat flow density determination*. Kluwer, Dordrecht, pp 447–468